

Permeability, Relative Permeability, Microscopic Displacement Efficiency, and Pore Geometry of M₁ Bimodal Pore Systems in Arab D Limestone

Edward A. Clerke, SPE, Saudi Aramco

Summary

Pore geometrical parameters for the M₁ petrophysical rock type of the Arab D limestone in Ghawar field have been related to static and dynamic reservoir properties and geological facies (Clerke et al. 2008). The M₁ bimodal pore system is the most common and important member of a new set of ultimate recovery petrophysical rock types (URPRT), which uses a new pore system classification for the Arab D limestone. The dynamic reservoir property results for the bimodal M₁ are reviewed here. The roles played by the pore system parameters describing the macropores (M) and micropores (Type 1) within the M₁ in permeability, imbibition oil relative permeability, and microscopic displacement efficiency are examined in detail. All pore systems are analyzed by the Thomeer method using an extensive mercury injection capillary pressure (MICP) data set in conjunction with dynamic experiments performed on samples prepared using the same wettability restoration. Effects commonly ascribed to wettability changes are observed by changes in the distribution of porosity between the M and Type 1 subsystems.

An extensive study of the pore systems of the Ghawar Arab D limestone gathered a large and comprehensive MICP data set (484 samples) (Clerke et al. 2008; Cantrell and Hagerty 1999, 2003; Clerke 2003, 2004; Ahr et al. 2005). All MICP data were type-curve matched by Thomeer functions (Clerke et al. 2008; Thomeer 1960). The study of this carefully prepared MICP data is the foundation for a new pore system classification. The new classification is built upon intrinsic, fundamental, and separate maximum pore-throat diameter modal elements named “porositons” (Clerke 2008; Ahr et al. 2005). Porositons are stable and recurring modes in the statistics of the Thomeer maximum pore-throat diameter of these carbonate pore systems. Porositon combinations are used to construct meaningful petrophysical rock types. Petrophysical rock types (PRTs) are defined by Clerke et al. (2008) as objects or combinations of objects that are present in the 3D space of the Thomeer pore-system parameters. Porositons are a new PRT object type; other PRT objects are clusters, trends, and surfaces. By constructing PRTs from porositons, strong relationships are found connecting the geological facies, PRTs, and reservoir-flow properties of these complex multimodal carbonate rocks (Clerke et al. 2008). These relationships demonstrate that these PRTs are important for defining ultimate recovery.

Introduction

Extensive and detailed pore system studies have been reported on the Arab D limestone pore systems in a major oil reservoir in Saudi Arabia (Clerke et al. 2008). That study created connections between the three major languages of the subsurface: depositional geological facies, petrophysical rock types, and reservoir static and dynamic properties (Clerke et al. 2008; Cantrell and Hagerty 1999, 2003; Clerke 2003, 2004; Ahr et al. 2005; Thomeer 1960) as

required for integrated reservoir characterization. The connections were made possible by a fundamentally significant observation regarding the limestone pore system geometries.

The spectrum of maximum pore-throat diameters ($\text{Log } P_d$) captured in this large MICP data set exhibited four distinct Gaussian modes that have been termed “porositons” (Fig. 1). PRTs are defined as combinations of porositons. Porositons are distinct and separable maximum pore-throat size distributions that are based on the four Gaussian modes in the $\text{Log } P_d$ or maximum pore-throat diameter frequency spectrum.

The studies indicate that a major portion of the depositional facies and pore volume can be identified with one PRT—M₁, the Macroporositon/Type 1 microporositon combination.

The prevalent M₁ PRT is a bimodal pore system consisting of an instance from the distribution of Macro possibilities (M porositon) and an instance from the Type 1 microporositon distribution. The M instance comes from the wide range of maximum pore-throat diameters within the M porositon. The Type 1 instance comes from a narrow range of smaller maximum pore-throat diameters within the Type 1 microporositon. The maximum pore-throat diameters of the Type 1 microporositon are, on the average, 53 times smaller than the M macroporositon average maximums. The Thomeer analyzed MICP data indicate that 17% is the average amount of porosity classified as M with a mean maximum pore-throat diameter of 58 μm . For Type 1 microporosity, 5.6% is the average pore volume with a mean maximum pore-throat diameter of 1.1 μm (Clerke 2008). Both pore subsystems are well connected to themselves and each other. Thus, commonly and widely present in our Arab D reservoir is a bimodal M₁ pore system with a very large contrast between a fine network of well-sorted small-diameter tubular intraparticle Type 1 pores connected and adjacent to much larger diameter moderately sorted interparticle M macropores. At many reservoir elevations, oil is present in both pore subsystems. When oil is present in both subsystems, the oil in the Type 1 micropores has been emplaced at a significantly higher capillary pressure than that required to emplace a much larger volume of oil into the large M macropores. This large contrast between the mean maximum pore-throat diameters of the M and Type 1 pore subsystems and the related capillary entry pressure contrast results in strong partitioning of the roles played by the two subsystems in the dynamic reservoir properties.

This porosity partitioning is first made manifest in a new M₁ permeability model, which uses information primarily from the M porositon. The shape of the oil imbibition relative permeability curve is also shown to be controlled by the M porositon through the M-controlled permeability in samples prepared with the same wettability restoration. However, properties of both M and Type 1 pore subsystems are necessary to completely characterize the full M₁ imbibition oil relative permeability behavior in terms of initial and final saturations.

Our pore-geometrical driven calculations use only the permeability (M attribute) and reproduce the single point normalized laboratory imbibition oil relative permeability over a range from 1 to 0.001 for seven out of eight waterflood composites. Unnormalized core plug centrifuge relative permeabilities variations are accounted for by including properties of the Type 1 micropores. Increasing

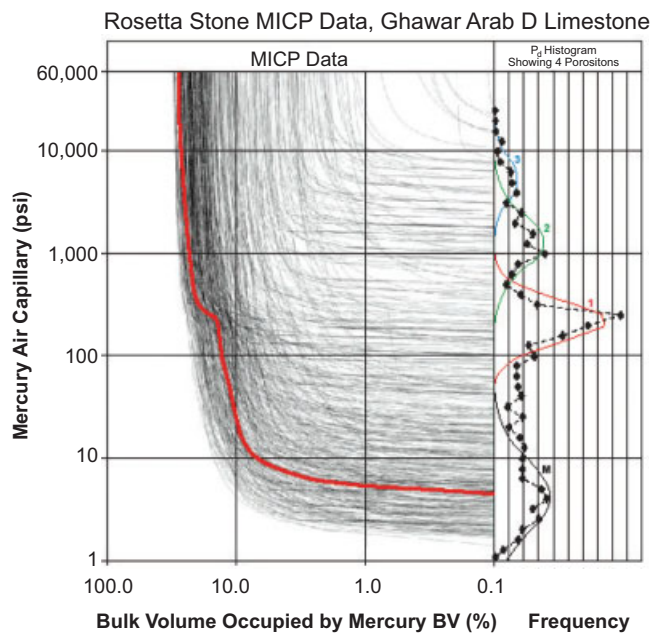


Fig. 1—Rosetta Stone MICP data after closure correction and Thomeer analysis with a histogram of the extracted entry pressures shown as black diamonds. The modes in the entry pressure (maximum pore-throat diameter) spectrum can be fit by four normal (Gaussian) distributions to an r^2 of 0.85. The macro mode is in black on the right, with Type 1 microporosity in red, Type 2 microporosity in green and Type 3 microporosity in blue. Full discussion of this data is in the work by Clerke et al. (2008). One of the prevalent bimodal capillary pressure curves, M_1, is highlighted in red.

amounts of Type 1 microporosity within the M_1 core plugs are related to shifts of the oil relative permeability curve to increasing water saturation and reduced residual oil saturation. These varying microporosity volumes produce an intrinsic “ineffective” water saturation offset to the relative permeability curve in these data. To widely implement our new approach to relative permeability in the M_1 reservoir intervals, we intend to investigate the possibility that the controlling pore subsystem properties could be extracted from appropriate processing of modern spectral porosity well log data (Allen et al. 2001; Newberry et al. 1996; Russell et al. 2004).

Background

Thompson et al. (1987) wrote a portentous review of the pore geometrical problems of sedimentary rocks noting, “Prediction of rock properties, such as the transport properties of fluids in the pore space, and the elastic properties of the grain space, requires a set of statistics that embody the relevant physics;” and “More generally, the statistical description of pore geometry awaits definition of relevant statistics. This approach could ultimately tie the geology of rock formation to their reservoir properties, a tie with important consequences for oil exploration and production.”

Our pore system statistics for the M_1 Arab D limestone extracted using Thomeer (1960) analysis of MICP data, extend the pore system and petrographic observations of Cantrell and Hagerty (1999, 2003) into 3D statistical information encompassing petrophysical and dynamic reservoir properties. Our data-gathering methods emphasized high quality control in the assignment of geological facies (Clerke 2008) to the core plugs. Non-Thomeer behavior was only observed in core plugs that were mechanical composites of two distinct geological facies (Clerke 2008). The statistics of the maximum pore-throat diameters (which can be represented as mercury injection entry pressures, P_d) were neither random nor uniform but, instead, presented a spectrum that could be modeled by four distinct porositons (Ahr et al. 2005) (Fig. 1). The data and the porositon Gaussian mode fitting parameters are published in Clerke et al. (2008).

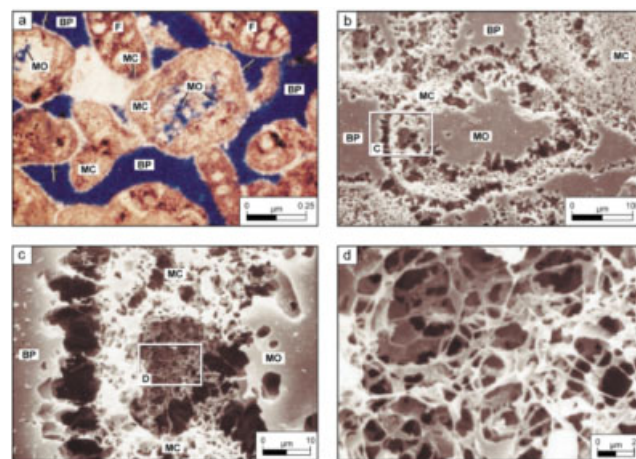


Fig. 2—Petrographic image of the Arab Formation limestone M_1 pore system after Cantrell and Hagerty (1999). Porosity is filled by blue dye in the upper left image. The succeeding scanning electron microscope images are of pore casts of increasingly higher magnification focusing on the Type 1 microporosity after removal of the carbonate matrix by acid. The microporosity is well connected. (Reproduced with permission of GeoArabia.)

Other 3D image quantification techniques, such as micro-CT, can resolve information only about the macropore system. The current micro-CT resolution limit of approximately $0.5 \mu\text{m}$ precludes the capture of microporosity network details (Arns et al. 2005). The petrographic investigations of Cantrell and Hagerty demonstrated the well-connected nature of the Type 1 micropores (Fig. 2). Type 1 micropores are tubular intraparticle micropores (Cantrell and Hagerty 1999, 2003) that are very uniform in maximum pore-throat diameter (see narrow Type 1 red peak in Figure 1) and very well sorted (low Thomeer G). The Type 1 pore-throat diameters and reservoir saturations indicate that they also contain reservoir oil at most reservoir elevations.

Previous workers using MICP data have identified internal substructures in the behavior of the filling of a pore system by mercury and coined terminology to describe those modes. Melrose (1965) identified a particular mode in the mercury filling, called “rheon.” Morrow (1970) introduced the mode term “ison,” and Yuan (1991) subdivided the ison into “rison” and “subison.” In our work, we observe structures in the statistics of the Thomeer parameters. Four modes, modeled with Gaussian distributions in the $\text{Log } P_{d,\text{max}}$ frequency spectrum, are observed in the maximum pore-throat diameter statistics. This is interesting and practical because, as the pore-throat diameter increases toward its maximum pore-throat diameter value, it approaches the magnitude and perhaps the behavior of the pore bodies. Hence, maximum pore-throat diameter behavior and pore-body behavior may be closely related (Clerke 2008). Pore-body information is inferred by nuclear magnetic resonance (NMR) measurements. More observations on the maximum pore-throat diameter (MICP) to NMR pore-body relationships in these samples are presented in Clerke et al. (2008) and are a subject of active investigation.

Thompson et al. (1987) emphasized the importance of properly characterizing the statistics of the pore system attributes. He also noted that “within the many studies of pore networks composed of pipes of widely varying sizes, which are distributed randomly along the links of the network, ... there are no experimental data to contradict the assumption of random distribution of pores.” Our data (Clerke 2008) is likely the first and the most comprehensive data to show a deeper and nonrandom structure in the pore network parameters of the Arab D limestone. Our studies (Clerke 2008) also indicate that a major portion of the depositional facies: Cladocoropsis, Stromatoporoid/Red Algae/Coral, and Skeletal/Oolitic, and a large portion of the reservoir pore volume can be identified with one particular macro/micro Type 1 (M_1) porositon combination (Fig. 1). The static and dynamic properties of the prevalent

bimodal M₁ pore systems are very important for forecasting Arab D limestone reservoir performance.

Permeability of Multimodal Pore Systems in Arab D Limestone

Multimodal pore systems are common in our Ghawar Arab D limestone MICP data (Clerke 2008). Multimodality refers to the number of Thomeer hyperbolas required to fit the MICP data of one core plug sample, each of which had been thoroughly inspected to be a member of only one geologic facies (Clerke 2008). Up to three Thomeer hyperbolas per sample were required, hence the sample modality nomenclature: monomodal for one Thomeer hyperbola, bimodal for two Thomeer hyperbolas, and trimodal for three Thomeer hyperbolas. Only the porosity containing the largest pore-throat diameters (in this case, the M porosity in the M₁ bimodal) in these multimodal pore systems contributes to the measurable total sample permeability. Use of the Thomeer permeability algorithm (Thomeer 1983) demonstrates that the first pore system contains all of the information regarding measurable permeability. Thomeer published an algorithm for the air permeability using the three Thomeer parameters derived from matching MICP data to a Thomeer hyperbola (Thomeer 1960, 1983):

$$K_a \text{ [md]} = 3.8068 G^{-1.3334} (B_{v,\infty} / P_d)^2 \dots \dots \dots (1)$$

The calculated Thomeer permeability value is compared to the measured value for over 400 samples (Clerke 2008), of which 18% are trimodal, 53% are bimodal, and 29% are monomodal, using only the Thomeer parameters from the first pore system (Fig. 3). The results show excellent comparison to data from 0.1 md to nearly 10 darcy using logarithmic axes. [Multimodal samples are very common in rocks with permeability greater than 10 md (Clerke 2008).] The agreement with the measured permeability is well within the claimed uncertainty (Thomeer 1983) (1.82x) of the Thomeer algorithm and far exceeds conventional porosity/permeability approaches, which may have two and a half orders of magnitude uncertainty.

Now, focusing on the Thomeer parameters of only the M pore system, the explicit dependence of the permeability upon each individual Thomeer parameter is investigated. The three Thomeer parameters are (Thomeer 1960) P_d , G , and $B_{v,\infty}$, which parameterize the minimum entry pressure directly related to the maximum pore-throat diameter P_d , the uniformity (low G) or nonuniformity (high G) of the pore-throat diameters, and the pore volume in that particular Thomeer hyperbola $B_{v,\infty}$, respectively. In our data, the major control on permeability is exhibited by the Thomeer parameter, P_{df} , which is indicative of the diameter of the maximum

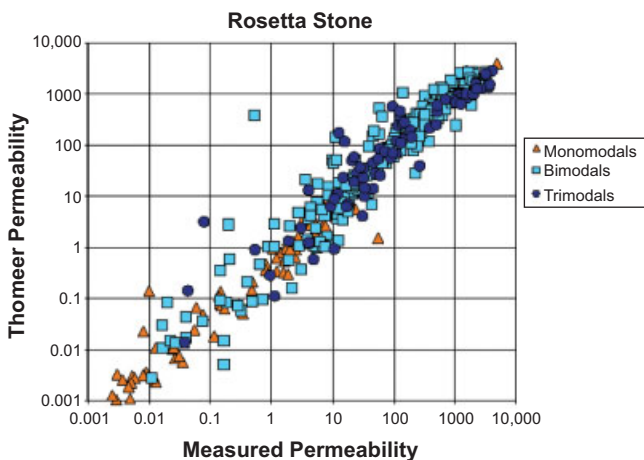


Fig. 3—Permeability computed by the Thomeer algorithm using the parameters only from the first pore system in multimodal samples vs. measured permeability for 484 limestone samples within the Rosetta Stone data set. Monomodals (orange triangles), bimodals (light blue squares), and trimodals (dark blue squares) are shown.

pore-throat in the first (lowest entry pressure, $f = M$ for the M₁) pore system (Fig. 4). For reference, the conversion from pressure to pore-throat diameter is given by the Young-Laplace equation (Adamson 1990):

$$P_c = \frac{0.58\sigma \cos\theta}{d} \dots \dots \dots (2)$$

for a mercury/air system, where $\theta = 140$ degrees, $\sigma = 480$ dynes/cm, pore-throat diameter d is in microns and P_c is in psia, yielding for the largest pore throat $d_{throat, max}$ and the initial entry pressure P_{df}

$$d_{throat, max} \text{ [microns]} = 214/P_{df} \text{ [Hg/air psi]} \dots \dots \dots (3)$$

The strongest correlation is between permeability and P_{df} , $r^2 = 0.65$. Another good correlation is between permeability and the total porosity, $r^2 = 0.55$. Neither parameter by itself is sufficient to establish a very high quality prediction for permeability.

Two-Term Permeability Equation for M₁ Bimodal Pore Systems in Arab D Limestone

The Rosetta Stone MICP data (Clerke 2008) was then used to investigate simple two term permeability equations. TableCurve 3D software (Systat; San Jose, California; 2007) allows a rapid investigation of many equations in terms of the correlation quality. For ease of general implementation, I only discuss the use of the maximum pore-throat diameter and the total porosity. This high quality and simple two-term permeability model is (Fig. 5)

$$Z = a + bX + cY, \dots \dots \dots (4)$$

with $a = -1.54$, $b = 1.20$, and $c = 0.073$ using the variables $X = \text{Log}_{10}$ (maximum pore-throat diameter in microns = $214/P_{df}$); $Y = \text{porosity in percent}$; $Z = \text{Log}_{10}$ (measured permeability); and the overall correlation r^2 is 89%. The result is shown in Fig. 5; the yellow color points are within one standard deviation of the fit surface and the dark blue points are within two standard deviations.

The measured vs. predicted plot for this simple two-term permeability model gives an excellent result over seven orders

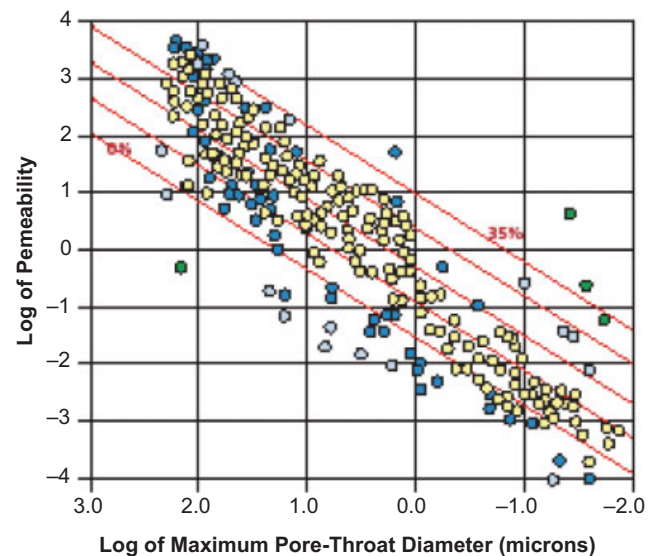


Fig. 4—Permeability vs. maximum pore-throat diameter data are shown on a log-log scale with a red background implicit porosity grid for porosities from 0 to 35%. Correlation with maximum pore-throat diameter is good, but neither parameter by itself is sufficient to establish a very high quality prediction for permeability. Yellow points are within one standard deviation of a 2D surface fit shown in Fig. 5. Dark blue points are within 2 standard deviations. Light blue points are outside 2 standard deviations. (Reproduced with permission of GeoArabia.)

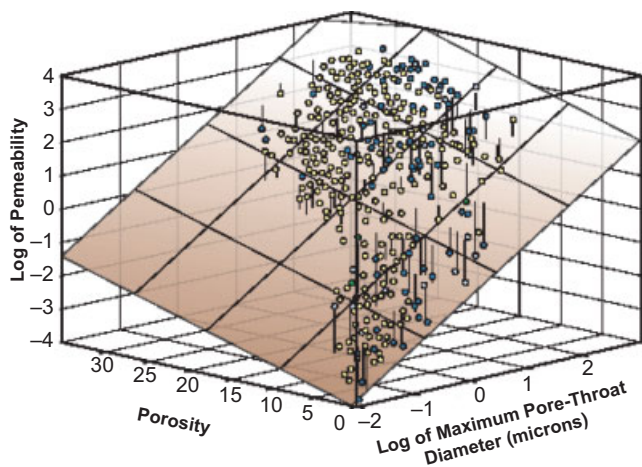


Fig. 5—3D view of the 2D surface fit to compute permeability from maximum pore-throat diameter and porosity in TableCurve3D (Systat; San Jose, California; 2007). Yellow points are within one standard deviation of the 2D surface fit. Dark blue points are within 2 standard deviations. Light blue points are outside 2 standard deviations. (Reproduced with permission of GeoArabia.)

of magnitude (Fig. 6). A two-term algorithm is similar to the approach of Lucia (1995) who proposed a two-variable pore-space to permeability model using the particle size and the interparticle porosity for non-vuggy rocks. Instead of the particle size, we use the maximum pore-throat diameter. The two input parameters, total porosity, and maximum pore-throat diameter of the first pore system are under investigation for determination from conventional porosity well logs along with spectral porosity data from NMR and electromagnetic imaging well logs (Allen et al. 2001; Newberry et al. 1996; Russell et al. 2004).

Imbibition Oil Relative Permeability and Microscopic Displacement Efficiency of M_1 Bimodal Pore Systems in Arab D Limestone

The previous section discusses that the M porosity carries more than 99% of the permeability information in these M_1 rocks (Clerke 2008). The contribution of the microporosity to the overall pore system permeability is very small and below the reproducibility of the permeameter measurement. If it is true that the M porosity is the major control on measured permeability, then it must also be the major control on the relative permeability curve among samples with a common wettability. Conversely, the Type 1 microporosity saturations must contribute to the relative permeability data in some alternate fashion. In drainage, the large capillary diameter differences between the M and Type 1 pore systems will result in significant partitioning of the two liquid saturations (oil and water). When a pressure gradient is applied, as in forced imbibition, the bulk of Darcy-type flow (99%) will occur within the M part of the pore system. In contrast, the small diameter Type 1 micropores will provide significant capillary forces to the system along with an imperceptible contribution to flow. The small pore throats and tubular weblike nature of the Type 1 network (Fig. 2) suggest that these micropore systems are much more likely to be water wet than macropores at equivalent reservoir elevations. The low curvature (large diameter) surfaces of the M pore systems are likely to have significant areas that are oil wetted. Hence, bimodality is related to mixed wettability. It can be shown that the partitioning of the pore space by the entry pressure (drainage) classification (porosities) is also related to partitioning behavior in the imbibition properties.

To investigate two-phase flow in our bimodal pore system in the absence of wettability effects, I modify a mathematical device by Purcell. Purcell (1949) proposed a simple model of a pore system as consisting of a bundle of tubes of varying radii and volumes.

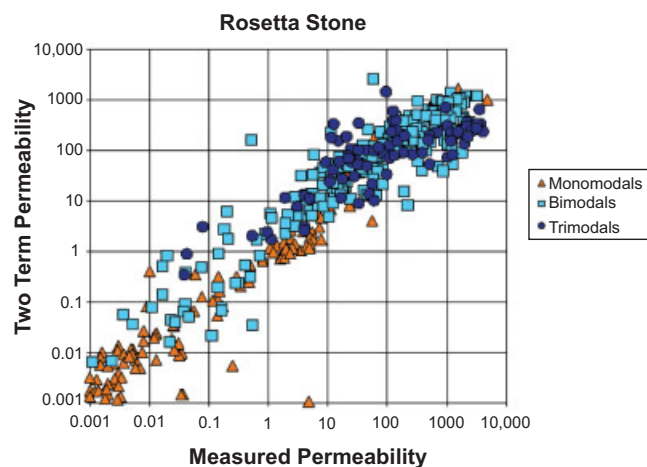


Fig. 6—The permeability computed using the new two-term permeability equation vs. measured permeability for 436 samples from the Rosetta Stone data set. Monomodals (orange triangles), bimodals (light blue squares), and trimodals (dark blue circles) are shown.

He proceeded to calculate the contribution to the permeability that each tube makes as a function of its radius ($\sim 1/P_c$) and volume when filling is by the (strongly nonwetting) intrusion of mercury. His model leads to a straightforward calculation of the contribution to permeability of each tube in the tubular bundle to the total permeability. Purcell (1949) states

$$K \propto \int_{S_{\text{nonwet}}=0}^{S_{\text{nonwet}}=100\%} \frac{dS_{\text{nonwet}}}{P_c^2} \dots \dots \dots (5)$$

I apply a series of these Purcell integrals (Purcell 1949) to our MICP data (P_c, S_{nonwet}) with a steadily increasing upper limit of integration. For my series of Purcell integrations, I steadily increase the upper limit of integration, S_{nonwet} , from zero to 100%, to produce a series of mathematical calculations for the mercury (to air) drainage (strongly nonwetting) relative permeability, K_{MDRP} . As the upper limit approaches $S_{\text{nonwet}} = 100\%$, then K_{MDRP} must reach the Purcell permeability value, K . In symbols, we have that as $S_{\text{nonwet}} \rightarrow 100\%$,

$$\text{for } K_{\text{MDRP}} = \int_{S_{\text{nonwet}}=0}^{S_{\text{nonwet}}} \frac{dS_{\text{nonwet}}}{P_c^2}, \text{ then } K_{\text{MDRP}} \rightarrow K.$$

More importantly, the calculation of my series of Purcell integrals results in a graph of the strongly nonwetting K_{MDRP} curve arising from the accumulating MDRP permeability as mercury (nonwetting) saturation increases by successively accessing tubes starting with the largest diameter.

Results from this MDRP curve calculation on both monomodal and bimodal capillary pressure data are compared. For a group of monomodal M samples represented by one particular sample of 18% porosity and 28 md permeability, the MDRP permeability accumulation is essentially complete at approximately 50% of the total M porosity (Fig. 7). Similarly, the MDRP permeability accumulation for the bimodal M_1 in Fig. 8 (22% porosity, 34 md permeability) is complete at approximately 8% porosity, which is approximately 50% of the M porosity (the high pressure extrapolation of the lower pressure first Thomeer hyperbola of approximately 18%). The MDRP permeability accumulations demonstrate that permeability is dominated by the macroporosity (large tubes) and less than the largest 50% of the M porosity as ranked by decreasing M pore-throat diameters.

The Type 1 microporosity contributes in a different way. This is examined using sets of special twin plugs from another MICP data set (Hagerty and Cantrell unpublished). These special twin pore systems have nearly the same porosity and permeability but differ in the presence/absence of microporosity. In Figs. 9 and 10, the capillary pressure curves for the M_1, Sample 307, and M,

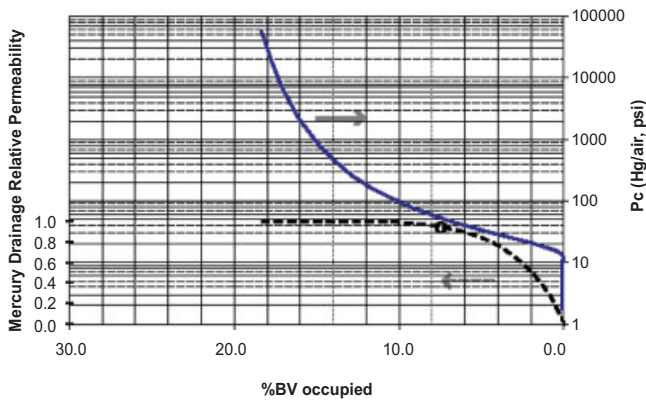


Fig. 7—The mercury injection capillary pressure curve (solid) and a Purcell MDRP permeability calculation (dash) for a monomodal M pore system. The circled point indicates the 90% buildup of permeability occurs at approximately 8%, (%BV occupied) and the sample has an ultimate %BV occupied of approximately 19%. Hence, the 90% permeability buildup occurs at less than 50% M saturation.

Sample 309, special twin samples are displayed along with the calculated MDRP permeability accumulation curves. Sample 307 has microporosity, and Sample 309 does not. The MDRP permeability accumulation shows that the major difference in the two MDRP curves is in the value of the saturation at which K_{MDRP} reaches 1.0. The saturation at which K_{MDRP} reaches 1.0 for the microporous sample (M_1, Sample 307) is shifted to the right or toward increased wetting-phase saturation as compared to the monomodal (M, Sample 309). The relative increase of the wetting-phase saturation or saturation-offset is caused by the “permeability-ineffective” saturation of the capillary-dominated Type 1 micropores.

New Pore Geometrical Model of Imbibition Relative Permeability Data for Multimodal Pore Systems in Arab D Limestone

Actual oil/water imbibition (brine saturation increasing) relative permeability experiments using M_1 rock types were acquired using the steady-state method in 1994 and were re-examined to investigate this saturation offset and the relationship to the presence of Type 1 microporosity. That study (an unpublished Aramco internal report) performed high-quality relative permeability measurements on eight composite M_1 cores from two Arab D cored wells. The steady-state

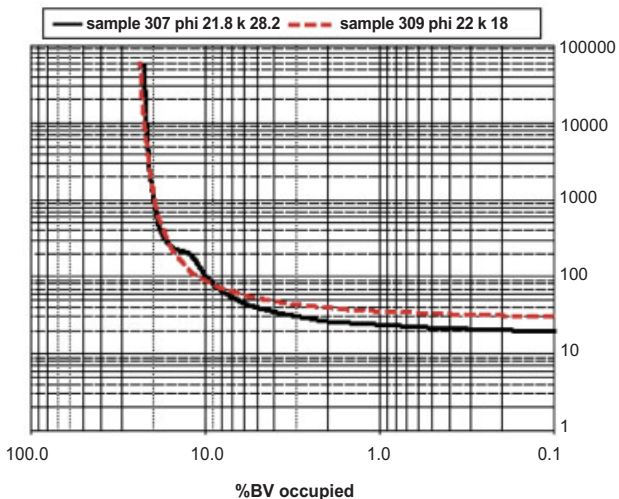


Fig. 9—Samples 307 (bimodal, solid line) and 309 (monomodal, red dashed line) MICP data with similar porosities (22% and permeabilities (28 and 18 md, respectively) but with and without Type 1 microporosity. Sample 307 has a micropore system into which mercury starts to enter at approximately 200 psi Hg/air.

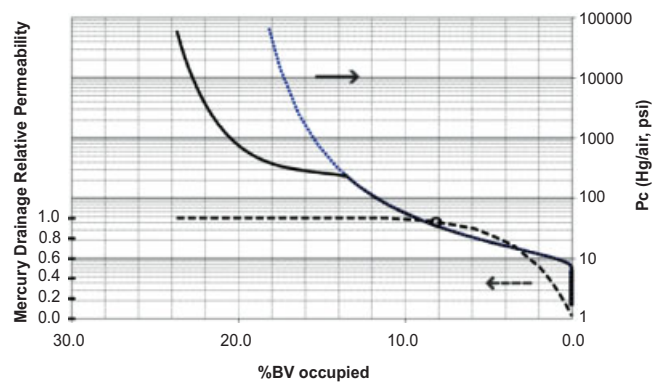


Fig. 8—The mercury injection capillary pressure curve (black solid and short-dash line, blue dashed line showing the extension of the macropore system) and a Purcell MDRP permeability calculation (long-dash line) for a bimodal M_1 pore system. The 90% buildup of permeability occurs at approximately 8%, (%BV occupied) and the sample has an ultimate %BV occupied for M of approximately 18%. Hence, the 90% permeability buildup also occurs near 50% M saturation in the M_1 system.

experiments used live reservoir fluids (recombined Abqaiq crude and live synthetic brine) and restored core conditions at reservoir temperature (210° F) and pressure (fluid at 3,300 psig and net confining stress of 3,100 psi). The cores were also under reservoir stress approximating that of the reservoir (Shafer et al. 1990; Braun and Blackwell 1981; Johnson et al. 1959). Matched core plugs were used in each composite (Huppler 1969). These floods were followed by centrifuge imbibition oil relative permeability and imbibition capillary pressure tests on the individual preserved core plugs from four of the eight composites. Centrifuge tests were made at 160° F and 3,100 psig net overburden. The steady-state imbibition oil relative permeability data were refined and extended by D.H. Jones in 2002 using both the centrifuge data and the steady state data (Fig. 11) and is used here. The resulting K_{ro} curves all have very similar shapes, and a cursory inspection seems to indicate a left-right translation or saturation-offset behavior. This saturation-offset behavior was previously shown to occur in the special twin samples as the amount of microporosity varied and affected the MDRP permeability accumulation.

To examine the data more closely, the extended and refined composite data were offset to a common origin, K_{ro} of 1 at $S_w - S_{w,max}$ ($K_{ro} = 1$), and the saturation-offset values tabulated; this was done to separate the differences related to saturation-offset and slope-curvatures. Once offset to a common origin (Fig. 12), the

Computed Mercury Relative Permeability for 307, 309 Special Twins

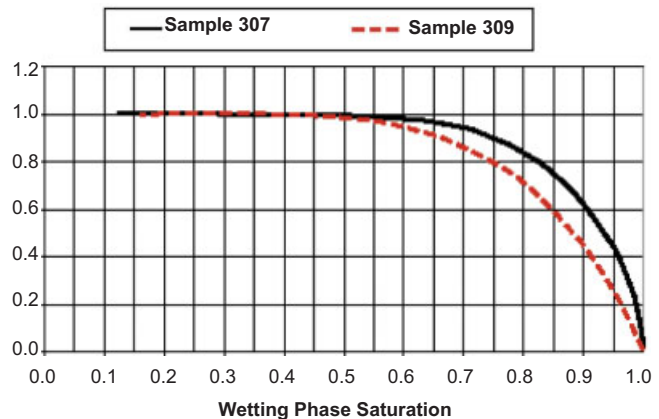


Fig. 10—Computed MDRP permeability curves for the two samples—307, M_1 bimodal (black line), and 309, M monomodal (red)—show a systematic shift to the right of the MDRP permeability curve in the presence of Type 1 microporosity (Sample 307) relative to the monomodal (Sample 309).

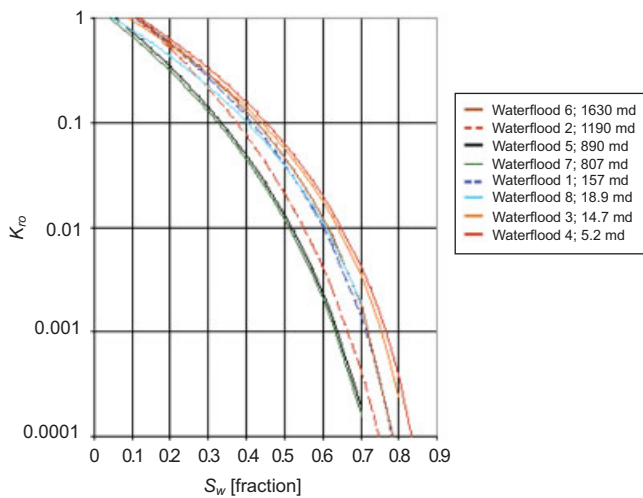


Fig. 11—Imbibition oil relative permeability curves for 8 M₁ composite core waterfloods, 1994 study, refined and extended by D.H. Jones. The intercepts at $K_{ro} = 1$ define the values of $S_{w,max}$ ($K_{ro} = 1$).

imbibition relative permeability data are easily observed to steepen with increasing absolute permeability. To parameterize this behavior, these offset data (single point normalization) were fit over their whole range to high accuracy using the function

$$\ln(K_{ro}) = a(e^{-y}-1) + b(y/\ln y), \dots \dots \dots (6)$$

with $y = S_{w,offset}$ (Fig. 12), where the data were offset using the intercepts shown on Fig. 11.

$$S_{w,offset} = S_w - S_{w,max} (K_{ro} = 1). \dots \dots \dots (7)$$

The fit coefficients a and b (Fig. 13) were observed to steadily increase with the permeability of the composites, which is the fit parameter manifestation of the steepening behavior shown in Fig. 12. Using the a and b regressions and the permeability value at $S_{w,ir}$, we reconstruct the oil relative permeability data vs. $S_{w,offset}$ (Fig. 14). The new function using the a and b regression equations agree with the data very well over three orders of magnitude in oil relative permeability, with the exception of waterflood Composite 6.

For a complete (denormalized) reconstruction of the restored state imbibition oil/water relative permeability data, it remains to understand and parameterize the S_w offsets (i.e., the $S_{w,max}$ ($K_{ro} = 1$) intercept values that were used for the single point normalization). Within the 1994 relative permeability study on M₁ pore systems,

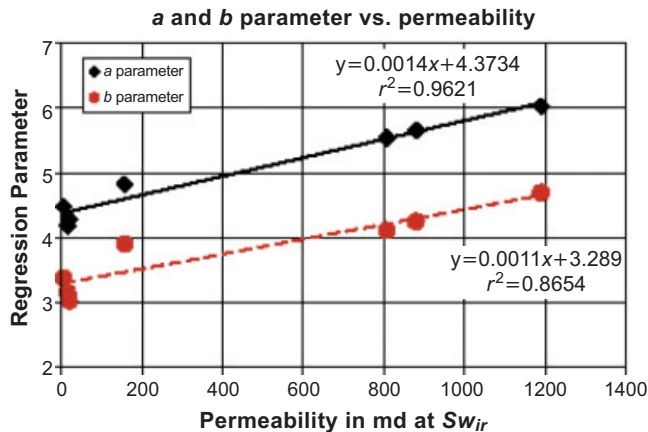


Fig. 13—The a (solid line) and b (dashed line) parameters in the imbibition oil relative permeability regression plotted vs. composite core permeability at $S_{w,ir}$. The values steadily increase with permeability.

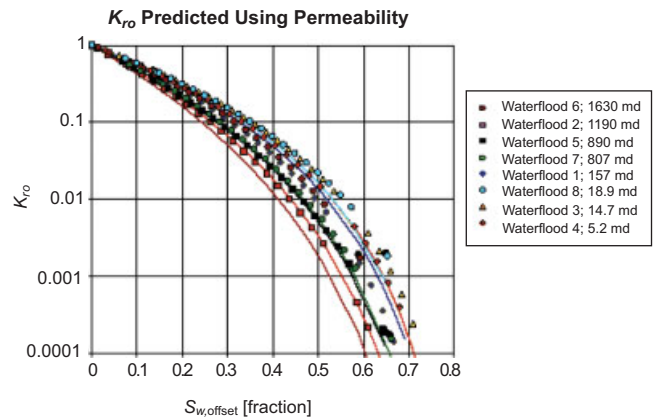


Fig. 12—Imbibition oil relative permeability data for eight M₁ waterfloods with fits to the data as lines. The imbibition oil relative permeability curves are offset to a common origin and are observed to steepen with increasing permeability.

one of the imbibition oil relative permeability composites provided the key. The waterflood Composite 3, like all of the composites, consisted of five matched core plugs with very similar porosities (~26%) and permeabilities (~10 md). Yet, the individual core plug centrifuge data obtained showed a very wide variation in the position of the oil relative permeability curve (Fig. 15). The significant offset differences in the individual centrifuge behavior of these five core plugs are not likely to be a result of the well matched porosity and permeability properties.

The MDRP permeability calculation exercise suggests that the offset in the relative permeability data arises from varying amounts of Type 1 microporosity in these core plugs. To test this, we investigate the correlation of the $S_{w,max}$ ($K_{ro} = 1$) intercept value to the quantitative presence of Type 1 microporosity. The plugs had MICP data from each plug end, which was analyzed for pore system Thomeer parameters (Clerke 2008; Thomeer 1960). The comparison of the $S_{w,max}$ ($K_{ro} = 1$) intercept values with the Type 1 microporosity volumes is shown in Fig. 16 for the five core plugs from Composite 3. The data is fit with a quadratic equation. The correlation is high and is in agreement with the results of the MDRP permeability calculation. The presence of an increasing volume of Type 1 micropores correlates with the steadily increasing water saturation offset of the actual reservoir fluids and the concomitant reduction of the residual oil saturation. The low initial water saturations for these plugs ensured that oil was in the Type 1 microporosity. The Type 1 microporosity is suggested to contribute to oil production through the spontaneous imbibition of water from and expulsion of oil to the adjacent M macropores. Additional data is being acquired to further investigate this behavior.

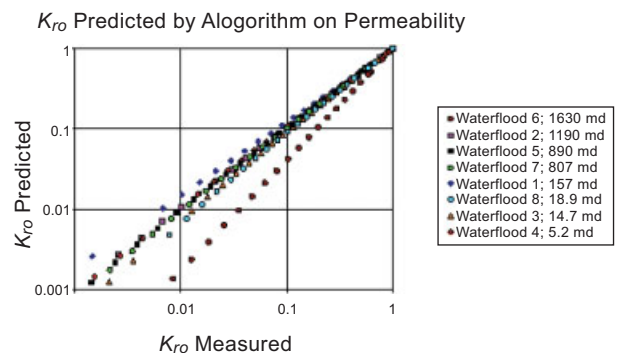


Fig. 14—Regression predicted offset imbibition oil relative permeability using only the independent parameter, permeability at $S_{w,ir}$ against the measured, refined, and offset values of Fig. 12. The regressions reproduce the data extremely well in all cases except for Waterflood 6.

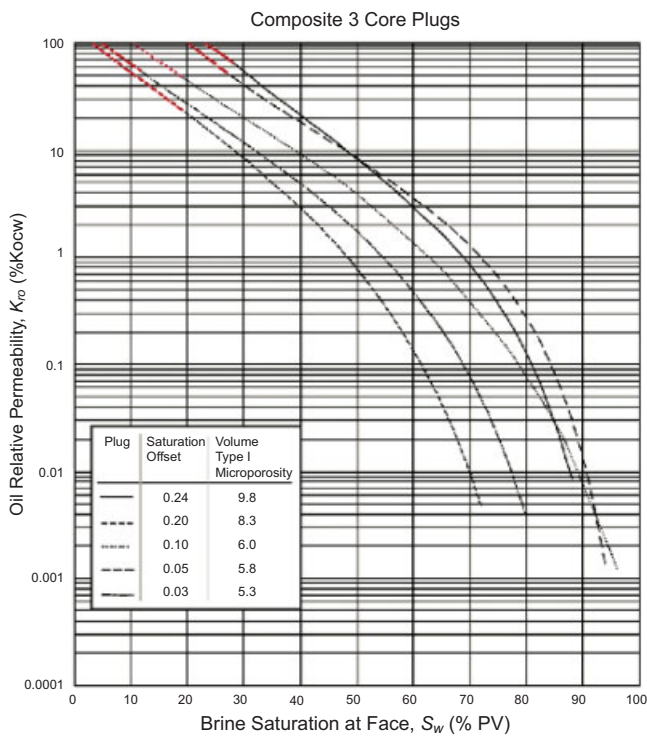


Fig. 15—The individual core plugs from Composite 3 showed variable water saturation offset behavior in their individual centrifuge oil relative permeability despite being matched for porosity and permeability. Investigation of the MICP data by Thomeer analysis on the plug end trims shows a varying amount of Type 1 microporosity among the plug set. Note that the relative permeability curve shapes are similar for the plugs. The legend shows the water saturation offset shown by the red extension of the data and the Type 1 microporosity volumes for each plug.

Conclusions

The permeability of the Ghawar Arab D limestones is largely governed by the large pore-throat diameters of the M macroporosity, which commonly occurs along with some Type 1 microporosity to form the M_1 ultimate recovery petrophysical rock type. The M porosity is observed to carry substantially all of the measurable permeability, while the contribution of the microporosity to permeability is imperceptible. This explains the poor results that arise from the total porosity/permeability methods for this carbonate. For this carbonate, the porosity/permeability crossplot and its inherent scatter is recognized to result from not addressing two important pore system properties related and not related to permeability: the largest pore-throat diameter and the presence of permeability “ineffective” microporosity, respectively.

A new two-term permeability model is constructed with the dominant term being, $P_{d,p}$ or the maximum pore-throat diameter of the M pore system and the total porosity. Though other parameters could have been used as the second input besides total porosity, these two parameters are targets for determination using appropriately acquired and processed modern spectral porosity well log data.

Detailed analysis of the permeability accumulation for the M_1 bimodal reservoir rocks uses a series of Purcell integrals to calculate the mercury drainage relative permeability curve demonstrates that essentially all of the permeability and the shape of the relative permeability curve is controlled by the largest pore throats and volumes that occur in about half of the M pore volume. The shape (single point normalization) of the imbibition relative permeability curves for eight waterflood composites can be modeled using this same permeability for samples of a wide range of permeability and prepared using the same wettability restoration process. The relative permeability curve shows steepening with permeability.

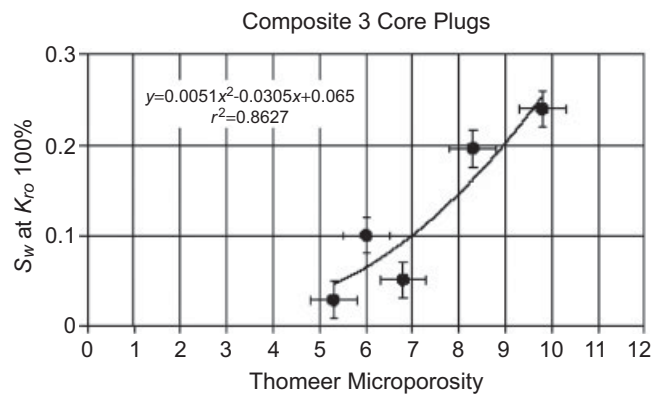


Fig. 16—The $S_{w,max}$ ($K_{ro} = 100\%$) offset value for each core plug in Composite 3 centrifuge oil relative permeability (Fig. 15) plotted against the amount of Type 1 microporosity as determined by the Thomeer analysis of the plug end MICP data.

The pore volume classified as Type 1 microporosity does not perceptibly contribute to the permeability as measured in current laboratory practice (~3 significant digits). It follows that if the micropores do not measurably contribute to the absolute permeability, their contribution is also not perceptible with two phase permeameters. The micropore volumes then do not contribute to the shape of the relative permeability curve. Instead, the increasing volumes of Type 1 microporosity in these experiments manifest themselves as an increasing intrinsic water saturation offset when imbibition is initiated and as a concomitant reduction of the residual oil saturation. Relative permeability data curves must be handled considering this microporosity effect before discussions about the wettability effects are meaningful for this petrophysical rock type. These conclusions about M_1 pore system behavior imply that:

- Flow test and flowmeter data from the Ghawar Arab D are dominated by the behavior of the first half of the very permeable M pore subsystem, and, therefore, flow is not necessarily indicative of the ultimate hydrocarbon recovery of the composite M_1 pore system. The flow response of the Type 1 microporosity is too small to be detectable in the presence of the large M permeability.
- Ultimate recovery forecasts based on fractional flow and relative permeability equations require specific knowledge of both the macro (M) and micro Type 1 pore systems. This important knowledge could be supported by obtaining information from appropriately processed NMR and electromagnetic imaging spectral porosity well logs in conjunction with conventional well logs.
- Reservoir monitoring must include detailed saturation determinations along with petrophysical rock type information that include the detailed characteristics of the M_1 bimodal pore systems.
- Ultimate recovery (dynamic) petrophysical rock types have been demonstrated for the limestones in this reservoir.

This work on the dynamic reservoir properties of the M_1 pore system when combined with previous work (Clerke 2008) demonstrate that these ultimate recovery petrophysical rock types can be linked to the geological rock types for integrated reservoir characterization of the Arab D reservoir. These results will greatly improve reservoir simulation studies for improving ultimate recovery.

Nomenclature

- B_v = percent of the bulk volume occupied by mercury
- $B_{v,\infty}$ = Thomeer parameter arising from the fit of a Thomeer hyperbola to MICP data, the asymptote of bulk volume occupied at infinite pressure
- d = pore-throat diameter, microns
- $d_{throat,max}$ = maximum pore-throat diameter arising from $P_{d,f}$, microns
- G = Thomeer pore geometrical factor
- K_a = air permeability, md

K_{MDRP} = calculated mercury to air drainage relative permeability (i.e., a permeability vs. saturation curve from a series of Purcell integrals operating on the MICP data and using a steadily increasing upper integration limit)

K_{ro} = relative permeability to oil

M = porosity with the largest maximum pore throat diameters, macroporosity

P_d = initial displacement pressure in which mercury starts to enter the pore system; a parameter arising from the fit of a Thomeer hyperbola to MICP data, psia, mercury to air

$P_{d,f}$ = initial displacement pressure of the first pore system, psia, mercury to air

S_{nonwet} = saturation of the nonwetting phase,

S_w = water saturation

$S_{w,ir}$ = irreducible water saturation

$S_{w,offset}$ = water saturation offset by $S_{w,max}$ ($K_{ro} = 1$) to bring the centrifuge K_{ro} curves to a common origin

$S_{w,max}$ ($K_{ro} = 1$) = value of the maximum S_w for which K_{ro} is still equal to one

$\sigma \cos \theta$ = surface tension times the cosine of the contact angle, dynes/cm

Acknowledgments

The author wishes to acknowledge the support and guidance of D.H. Jones, the Ghawar Integrated Assessment and New Technology (GIANT) team leader, and Nansen Saleri, under whom the bulk of this work was performed and whose support was greatly appreciated. Special thanks to the rest of the GIANT team and the multiorganizational management support received for this work from Saudi Aramco.

References

- Adamson, A.W. 1990. *Physical Chemistry of Surfaces*, 5th edition, 4–45. New York: John Wiley and Sons.
- Ahr, W.M., Allen, D., Boyd, A., Bachman, H.N., Smithson, T., Clerke, E.A., Gzara, K.B.M., Hassall, J.K., Murty, C.R.K., Zubari, H., and Ramamoorthy, R. 2005. Confronting the Carbonate Conundrum. *Oil-field Review* **17** (1): 18–29.
- Allen, D.F., Boyd, A., Massey, J., Fordham, E.J., Amabeoku, M.O., Kenyon, W.E., and Ward, W.B. 2001. The Practical Application of NMR Logging in Carbonates: 3 Case Studies. *Proc.*, SPWLA 42nd Ann. Logging Symp., Houston, 17–20 June, Paper K.
- Arns, C.H., Baugot, F., Limaye, A., Sakellariou, A., Senden, T., Sheppard, A., Sok, R.M., Pinczewski, V., Bakke, S., Berge, L.I. et al. 2005. Pore-Scale Characterization of Carbonates Using X-Ray Microtomography. *SPE J.* **10** (4): 475–484. SPE-90368-MS. DOI: 10.2118/90368-MS.
- Braun, E.M. and Blackwell, R.J. 1981. A Steady-State Technique for Measuring Oil-Water Relative Permeability Curves at Reservoir Conditions. Paper SPE 10155 presented at the SPE Annual Technical Conference and Exhibition, San Antonio, Texas, USA, 4–7 October. DOI: 10.2118/10155-MS.
- Cantrell, D.M. and Hagerty, R.M. 1999. Microporosity in Arab Formation Carbonates, Saudi Arabia. *GeoArabia* **4** (2): 129–154.
- Cantrell, D.M. and Hagerty, R.M. 2003. Reservoir rock classification, Arab-D reservoir, Ghawar Field, Saudi Arabia. *GeoArabia* **8** (3): 453–462.
- Clerke E.A. 2004. Beyond Porosity-Permeability Relationships—Determining Pore Network Parameters for the Ghawar Arab-D Using the Thomeer Method. Presented at the 6th Middle East Geoscience Conference and Exhibition, Manama, Bahrain, 7–10 March.
- Clerke, E.A. 2003. Beyond Porosity-Permeability Relationships: Determining Pore Network Parameters for the Ghawar Arab-D Using the Thomeer Method. *GeoFrontier* **1** (3).
- Clerke, E.A., Mueller, H.W. III, Phillips, E.C., Eyvazzadeh, R.Y., Jones, D.H., Ramamoorthy, R., and Srivastava, A. 2008. Application of Thomeer Hyperbolas to decode the pore systems, facies and reservoir properties of the Upper Jurassic Arab D Limestone, Ghawar field, Saudi Arabia: A “Rosetta Stone” approach. *GeoArabia* **13** (4): 113–160.
- Huppler, J.D. 1969. Waterflood Relative Permeabilities in Composite Cores. *J. Pet Tech* (May): JPT Forum, 539–540.
- Johnson, E.F., Bossler, D.P., and Naumann, V.O. 1959. Calculation of Relative Permeability from Displacement Experiments. *Trans.*, AIME, **216**: 370–372.
- Lucia, F.J. 1995. Rock fabric/petrophysical classification of carbonate pore space for reservoir characterization. *AAPG Bulletin* **79** (9): 1275–1300.
- Melrose, J.C. 1965. Interfacial Phenomena as Related to Oil Recovery Mechanisms. *Can. J. Chem. Eng.* **48**: 638–644.
- Morrow, N.R. 1970. Physics and Thermodynamics of Capillary Action in Porous Media. *Ind. Eng. Chem.* **62** (6): 32–56. DOI: 10.1021/ie50726a006.
- Newberry, B.M., Grace, L.M., and Stief, D.O. 1996. Analysis of Carbonate Dual Porosity Systems from Borehole Electrical Images. Paper SPE 35158 presented at the Permian Basin Oil and Gas Recovery Conference, Midland, Texas, USA, 27–29 March. DOI: 10.2118/35158-MS.
- Purcell, W.R. 1949. Capillary Pressures—Their Measurement Using Mercury and the Calculation of Permeability Therefrom. *Trans.*, AIME, **186**: 39–48.
- Russell, S.D., Sadler, R.K., Weihua, W., Richter, P., Eyvazzadeh, R., and Clerke, E.A. 2004. Applications of image log analyses to reservoir characterization, Ghawar and Shaybah fields, Saudi Arabia. GEO 2004 conference abstract, Bahrain, 7–10 March. *GeoArabia* **9** (1): 125.
- Shafer, J.L., Braun, E.M., Wood, A.C. III, and Wooten, J.M. 1990. Obtaining Relative Permeability Data Using a Combination of Steady-State and Unsteady-State Corefloods. Paper SCA 9009 presented at the Fourth Annual SCA Technical Conference, Dallas, 15–16 August.
- Thomeer, J.H. 1983. Air Permeability as a Function of Three Pore-Network Parameters. *J. Pet Tech* **35** (4): 809–814. SPE-10922-PA. DOI: 10.2118/10922-PA.
- Thomeer, J.H.M. 1960. Introduction of a Pore Geometrical Factor Defined by a Capillary Pressure Curve. *J. Pet Tech* **12** (3): 73–77; *Trans.*, AIME, **219**. SPE-1324-G. DOI: 10.2118/1324-G.
- Thompson, A.H., Katz, A.J., and Krohn, C.E. 1987. The microgeometry and transport properties of sedimentary rock. *Advances in Physics* **36** (5): 625–694. DOI: 10.1080/00018738700101062.
- Yuan, H.H. 1991. Pore-Scale Heterogeneity From Mercury Porosimetry Data. *SPE Form Eval* **6** (2): 233–240; *Trans.*, AIME, **291**. SPE-19617-PA. DOI: 10.2118/19617-PA.

Ed Clerke is a geological consultant in the Geological Modelling Division/Reservoir Characterization Department of Saudi Aramco. He holds a PhD degree in physics from the University of Maryland. Previously, Clerke has been head of petrophysics and petrophysical engineering advisor for Pennzoil E&P. He was also senior principal petrophysicist with ARCO E&P Technology and has held petrophysical engineering and research positions with Shell Oil Company USA. Clerke has published articles in *GeoArabia*, *SPE Journal*, *The Log Analyst*, *SPE Production Engineering*, *Physical Review*, *Physica*, and the *The Journal of Physical Chemistry*. He received the Best Paper Award at GEO 2006 and GEO 2004 for work presented on Arab D Limestone Pore Systems and received the 2006 Best Paper Award at the SPWLA Carbonate Permeability Topical Conference. Clerke received the 1993 Best Paper Award from the West Texas Geological Society for work in Permian Basin carbonates. He holds five patents, four in the area of downhole acoustic imaging technology.